Article

Transition from Sequential to Concerted Proton-Coupled Electron Transfer of Water Oxidation on Semiconductor Photoanodes

Siqin Liu,[§] Lei Wu,[§] Daojian Tang, Jing Xue, Kun Dang, Hanbin He, Shuming Bai, Hongwei Ji, Chuncheng Chen, Yuchao Zhang,* and Jincai Zhao

Cite This: *J. Am. Chem. Soc.* 2023, 145, 23849−23858

Read Online

ACCESS | ‖ Metrics & More | Article Recommendations | Supporting Information

ABSTRACT: Accelerating proton transfer has been demonstrated as key to boosting water oxidation on semiconductor photoanodes. Herein, we study proton-coupled electron transfer (PCET) of water oxidation on five typical photoanodes [i.e., α-Fe$_2$O$_3$, BiVO$_4$, TiO$_2$, plasmonic Au/TiO$_2$, and nickel−iron oxyhydroxide (Ni$_{1-x}$Fe$_x$OOH)-modified silicon (Si)] by combining the rate law analysis of H$_2$O molecules with the H/D kinetic isotope effect (KIE) and operando spectroscopic studies. An unexpected and universal half-order kinetics is observed for the rate law analysis of H$_2$O, referring to a sequential proton−electron transfer pathway, which is the rate-limiting factor that causes the sluggish water oxidation performance. Surface modification of the Ni$_{1-x}$Fe$_x$OOH electrocatalyst is observed to break this limitation and exhibits a normal first-order kinetics accompanied by much enhanced H/D KIE values, facilitating the turnover frequency of water oxidation by 1 order of magnitude. It is the first time that Ni$_{1-x}$Fe$_x$OOH is found to be a PCET modulator. The rate law analysis illustrates an effective strategy for modulating PCET kinetics of water oxidation on semiconductor surfaces.
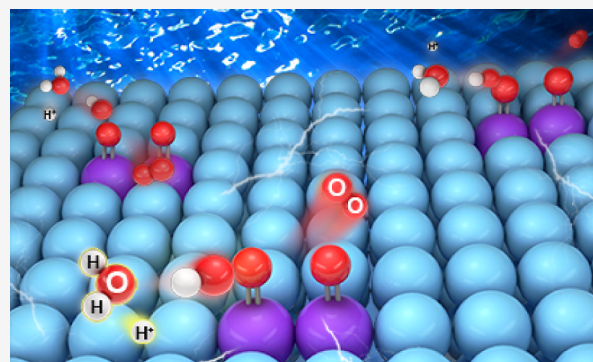
1. INTRODUCTION

Water oxidation is the bottleneck of overall water splitting. This reaction is a typical proton-coupled electron transfer (PCET) reaction, which involves the transfer of four electrons and four protons.[1−4] The PCET reaction can proceed by either a sequential proton−electron transfer (SPET) pathway or a concerted proton−electron transfer (CPET) pathway (Figure 1a), which greatly influences the kinetic barrier.[2,5−8]

Water oxidation is an important step in both natural and artificial photosyntheses.[9−13] In the natural world, the photosynthesis II (PSII) system is highly active and efficient for performing water oxidation, exhibiting a high turnover frequency (TOF) of >100 s^{-1}.[14−16] Proton transfer (PT) is effectively modulated by the surrounding amino acid residues as proton acceptors (e.g., Asp61, His190, Glu65) of the oxygen evolution center, which boost the electron transfer (ET) kinetics and result in the high TOF in the environment with relatively low water content.[7,17−20] For artificial photosynthesis, such as photoelectrochemical (PEC) water oxidation on semiconductor photoanodes, the reaction activities are much lower than for the PSII system.[12]

Previous studies propose the nonconcerted proton−electron transfers (i.e., SPET) for water oxidation when the pH-dependent activity on the reversible hydrogen electrode (RHE) scale appears,[21−23] wherein the water-oxidation activity can be further enhanced by increasing the pH of electro-

lyte.[22,24] A detailed theoretical study revealed that in a SPET pathway, PT has a significant activation energy of ∼0.2−0.5 eV, while the following ET is almost barrierless, which further explained the pH-dependent activity.[3] Despite this progress, a comprehensive understanding of PCET and effective strategies for modulating PCET kinetics of water oxidation on semiconductor surfaces remain to be developed.[8,21,25−27]

Rate law analysis of photogenerated holes has emerged as a powerful tool for the molecular-level understanding of water oxidation mechanisms on semiconductor surfaces.[24,28−32] For water oxidation on α-Fe$_2$O$_3$ photoanodes, the driving force for ET is reported to be manipulated by the accumulation of multiple oxidizing equivalents (i.e., high-valent iron oxo species, Fe^{IV}=O) on surfaces,[33] which is revealed by the rate law analysis of surface-trapped holes.[24,30,31] For the complete rate law formula of water oxidation (eq 1),[34,35] the rate law of H$_2$O should provide important implications for PT kinetics as the H$_2$O molecules act as both the substrate and proton acceptor during water oxidation.
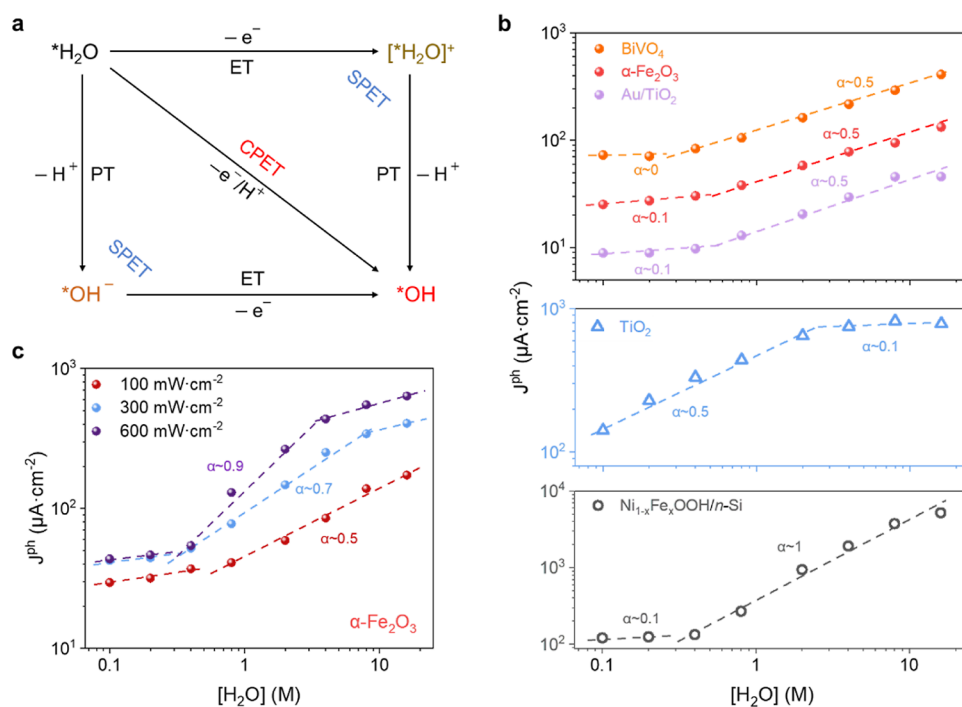
Figure 1. Rate law analysis of H_2O for water oxidation on five typical photoanodes. (a) Schematic of PCET pathways. ET and PT can proceed in a single step (CPET) or in sequential steps (SPET). (b) Log−log plot of the water oxidation reaction rate vs $[H_2O]$ in 0.1 M $TBAPF_6$ solutions at applied potentials of 0.8 V_{Ag/Ag^+} for $Ni_{1-x}Fe_xOOH/n$-Si, 0.4 V_{Ag/Ag^+} for TiO_2, and 0.6 V_{Ag/Ag^+} for α-Fe_2O_3 and $BiVO_4$ under AM 1.5 G illumination. Plasmonic Au/TiO_2 was measured at 0.6 V_{Ag/Ag^+} under a 470 nm LED of 100 mW cm^{-2} illumination. The potentials (vs Ag/Ag^+) were calibrated using a ferrocene/ferrocenium (Fc/Fc^+) redox couple in Figure S1. (c) Log−log plot of water oxidation reaction rate vs $[H_2O]$ in 0.1 M $TBAPF_6$ solutions at 0.6 V_{Ag/Ag^+} under 470 nm LED illumination of 100, 300, and 600 mW cm^{-2}, respectively. The dashed lines corresponded to the fitting of the rate law of H_2O (eq 1).

$$J^{ph} = k_{wo}[H_2O]^\alpha[h^+]^\beta \qquad (1)$$

where J^{ph} is the photocurrent density of PEC water oxidation, k_{wo} is the rate constant, α is the apparent reaction order of H_2O, and β is the apparent reaction order of surface holes.

However, the rate law of H_2O has seldom been explored for PEC water oxidation on semiconductor photoanodes because almost all previous heterogeneous semiconductor-based PEC water oxidation studies were performed in an aqueous solvent, in which the content of H_2O cannot be tuned. In contrast, most molecule-catalyzed homogeneous water oxidation studies were conducted in nonaqueous solvents, in which the rate law of H_2O has been studied.[36−38]

In this work, we conducted the rate law analysis of H_2O for PEC water oxidation on five well-known semiconductor photoanodes [i.e., α-Fe_2O_3, $BiVO_4$, TiO_2, plasmonic Au/TiO_2, and $Ni_{1-x}Fe_xOOH$-modified n-silicon ($Ni_{1-x}Fe_xOOH/n$-Si)] in mixed acetonitrile/water (CH_3CN/H_2O) solvent electrolytes and particularly focus on α-Fe_2O_3. A universal apparent reaction order of 0.5 was observed for H_2O during water oxidation on most of the above photoanodes except for $Ni_{1-x}Fe_xOOH/n$-Si. A SPET pathway was proposed to account for the half-order kinetics of H_2O, showing that H_2O is not a direct reactant in the water-oxidation reaction. But a prereaction step, H_2O dissociation, should take place before water oxidation occurs. This SPET pathway was the kinetic bottleneck for boosting water oxidation on photoanodes. For α-Fe_2O_3 photoanodes, further surface modification by using the $Ni_{1-x}Fe_xOOH$ electrocatalyst was found to exhibit an apparent reaction order of unity for H_2O and enhanced the TOF of water oxidation by 1 order of magnitude at high H_2O

concentrations ($[H_2O]$, 4−16 M). Combined with the H/D kinetic isotope effect (KIE), operando attenuated total reflectance Fourier-transform infrared (ATR−FTIR) spectroscopy, and surface interrogation scanning electrochemical microscopy (SI-SECM) measurements, a mechanistic transition from the SPET to the CPET pathway was revealed. It has been the first time that $Ni_{1-x}Fe_xOOH$ is found to be a PCET modulator. Besides, the PT process can be regulated by using the proton acceptor (pyridine), which significantly improved the TOF by nearly an order of magnitude at low $[H_2O]$ (0.1−0.4 M).

2. RESULTS AND DISCUSSION

2.1. Rate Law Analysis of H_2O. The dependences of water oxidation rate (J^{ph}) on $[H_2O]$ were explored on five typical photoanodes, that is, α-Fe_2O_3, $BiVO_4$, TiO_2, plasmonic Au/TiO_2, and $Ni_{1-x}Fe_xOOH$-modified Si (Figures 1b and S2). The apparent reaction order of H_2O is obtained via the $\log(J^{ph})$−$\log([H_2O])$ plot according to eq 1 assuming all other parameters remain almost unchanged during the measurement. The surface hole density was measured by electrochemical impedance spectroscopy (EIS) and transient photocurrent decay and was found to be almost constant at the $[H_2O]$ range of 0.8−16 M (for α-Fe_2O_3, $BiVO_4$, plasmonic Au/TiO_2, and $Ni_{1-x}Fe_xOOH/n$-Si) and at the $[H_2O]$ range of 0.1−2 M (for TiO_2), as shown in Figures S3−S6 (for detailed discussions, see Supporting Information Note 1). In addition, the reaction order of surface holes was found to remain constant at the $[H_2O]$ range of 0.8−16 M as described below. On the other hand, k_{wo} has always been assumed to remain unchanged at the
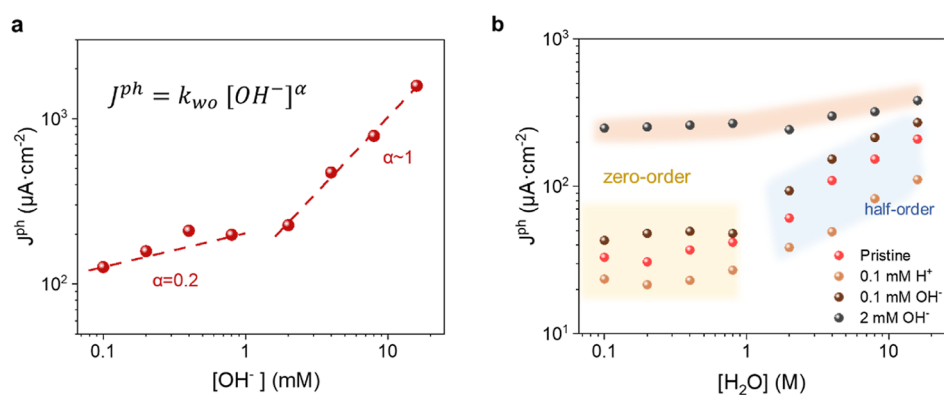
Figure 2. Rate law analysis of OH⁻ and the effect of proton concentration on the rate law of H_2O measured on the α-Fe_2O_3 photoanode. (a) Log–log plot of OH⁻ oxidation rate vs [OH⁻] in 0.1 M TBAPF₆ solutions under 470 nm LED illumination of 100 mW cm⁻² at a fixed applied potential of 0.6 V_{Ag/Ag^+}. The dashed lines corresponded to the fitting of the rate law of OH⁻ (the inset equation). (b) Log–log plot of water oxidation rate vs [H_2O] in 0.1 M TBAPF₆ solutions with 0.1 mM HClO₄, 0.1 mM TBAOH, and 2 mM TBAOH at a fixed applied potential of 0.6 V_{Ag/Ag^+}.

fixed applied potential and light intensity according to previous studies.[30,31]

Linear sweep voltammetry (LSV) curves of these photoanodes under illumination and in the dark are shown in Figures S7 and S8. Among the five materials, α-Fe_2O_3, $BiVO_4$, and plasmonic Au/TiO_2 photoanodes showed similar behavior, exhibiting a transition from quasizero-order (slope ~0.1) kinetics at low [H_2O] to a half-order (slope ~0.5) kinetics at high [H_2O] (Figure 1b), all of which were far away from unity or other integral numbers. The transition water concentration (TWC) was 0.8 M for α-Fe_2O_3 and plasmonic Au/TiO_2 and 0.4 M for $BiVO_4$ (Figure 1b). However, for the TiO_2 photoanode, a half-order kinetics appeared at low [H_2O] (0.1–2 M) and then the water oxidation rate remained almost unchanged at high [H_2O] (>2 M) (Figure 1b). All of these fractional apparent reaction order numbers of H_2O infer that the H_2O molecule is not the reactant that directly participates in water oxidation. A prereaction step, for example, H_2O dissociation, should take place before water oxidation occurs (for detailed discussions, see Supporting Information Notes 2 and 3).

Unlike most semiconductor photoanodes, n-Si photoanodes require the modification of an electrocatalyst layer to prevent the surface oxidation and further provide active sites for water oxidation.[39,40] Therefore, the $Ni_{1-x}Fe_xOOH$-modified n-Si (labeled as $Ni_{1-x}Fe_xOOH$/n-Si) photoanode was used herein. On $Ni_{1-x}Fe_xOOH$/n-Si, a first-order kinetics appeared when [H_2O] > 0.4 M, while quasizero-order kinetics was observed at low [H_2O] (Figure 1b). It is noteworthy that the similar first-order kinetics of H_2O was also observed on the $Ni_{1-x}Fe_xOOH$ electrocatalyst (Figure S9), indicating that the rate law of H_2O on the $Ni_{1-x}Fe_xOOH$/n-Si photoanode was determined by the surface $Ni_{1-x}Fe_xOOH$ electrocatalyst on which the H_2O molecule is indeed the reactant that directly participates in water oxidation.

The observed fractional and integral apparent reaction order numbers of H_2O suggest that there should be distinct reaction mechanisms for the H_2O molecule to participate in water oxidation (Supporting Information Note 2). The effect of the diffusion of H_2O molecules in a nonaqueous solvent on measuring the apparent reaction order was first considered. It is observed that varying the stirring speeds during photocurrent measurements had no influence on the results of the apparent reaction orders of H_2O (Figure S10a), indicating that

the diffusion of H_2O molecules was not the limiting factor in this reaction system. It is further confirmed by the LSV curves at various scan rates (Figure S10b–d) and the nondiffusion characteristics of Nyquist curves (Figure S10e,f) obtained by EIS measurements at different [H_2O]s. Besides, the effect of surface charge recombination should be considered. To illustrate the influence of surface recombination on the rate law analysis of H_2O, the triethylamine (hole scavenger) oxidation reaction and intensity-modulated photocurrent spectroscopy measurements were performed on α-Fe_2O_3 with [H_2O]s above 0.8 M, as shown in Figure S11. Based on the discussion in Note 1, the determination of the reaction order of H_2O was not affected by the surface recombination.

In the mixed CH_3CN/H_2O electrolyte, H_2O and OH⁻ (dissociated from H_2O) are the only two species that can be oxidized by photogenerated holes. The oxidation of OH⁻ is known to be energetically more favorable than the oxidation of H_2O (E_{O_2/OH^-} = 0.401 V and E_{O_2/H_2O} = 1.229 V_{RHE}).[41] Besides, previous theoretical calculations showed that the activation energies of direct oxidizing H_2O were substantially higher than oxidizing OH⁻ on α-Fe_2O_3 photoanodes.[32] When taking H_2O dissociation (from H_2O to OH⁻) into consideration, a fractional reaction order of H_2O is rational for the rate law analysis (see Supporting Information Note 2). This process can be considered as a SPET pathway, in which PT must occur prior to ET (Figure 1a).[5,6] In contrast, the integral reaction order of H_2O (~1 herein) indicates that the H_2O molecule directly take part in water oxidation and works via a CPET pathway, in which PT is concerted with ET (Figure 1a).[22] On the other hand, all five photoanodes showed quasi-zero-order kinetics at low [H_2O], implying that the oxidation of H_2O might not be the rate-determining step (RDS) under these circumstances, and other processes (e.g., surface hole-trapping process) mainly contributed to the observed photocurrent. The reaction mechanism at these low [H_2O] values is further discussed below.

In the following section, we particularly focus on α-Fe_2O_3 photoanodes for detailed studies. We confirmed the production of O_2 for water oxidation on the α-Fe_2O_3 photoanode at various [H_2O]s, showing a Faradaic efficiency of O_2 > 90% (Figure S12). Further increasing the light intensity improved the apparent reaction order of H_2O on α-Fe_2O_3 (Figure 1c), which reached ~0.9 when the light intensity was 600 mW cm⁻² at moderate [H_2O] (0.4–4 M).
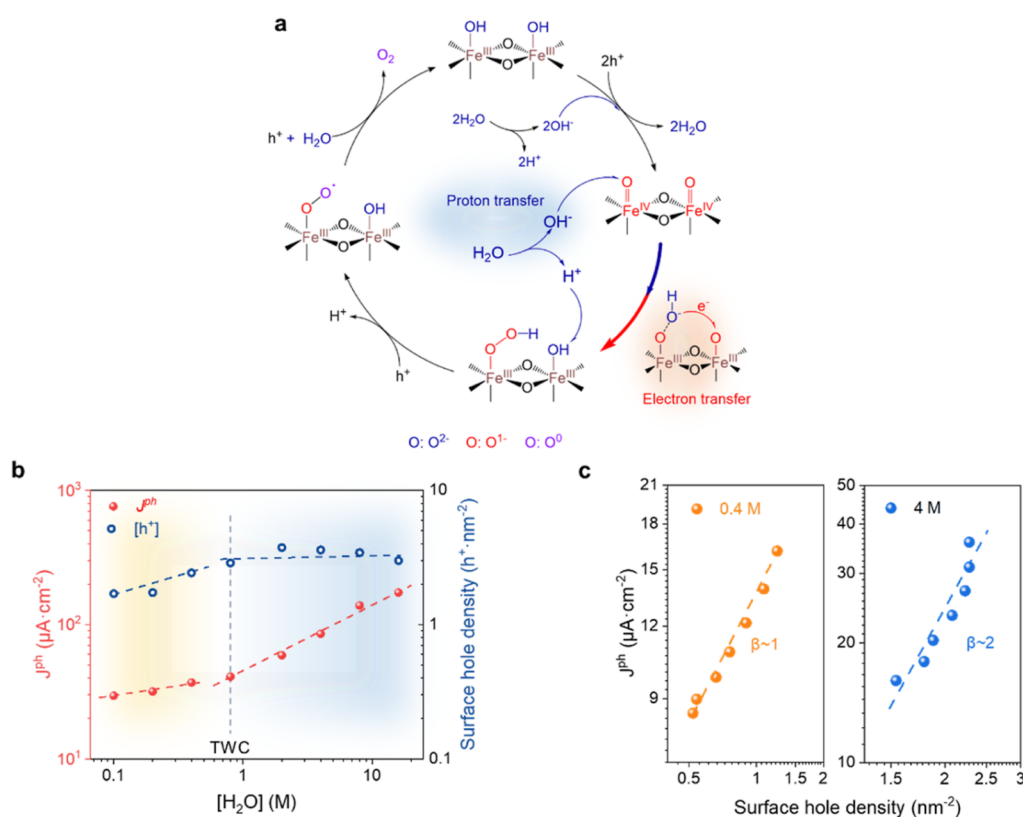
Figure 3. Surface hole density analysis based on EIS data on the α-Fe$_2$O$_3$ photoanode. (a) PCET pathways involved in water oxidation on α-Fe$_2$O$_3$. (b) Relationship between surface hole densities and [H$_2$O]s in 0.1 M TBAPF$_6$ with the applied potential of 0.6 V$_{Ag/Ag^+}$ under the 470 nm LED illumination of 100 mW cm^{-2}. The dashed vertical line indicates the TWC values. The fitted EIS parameters and calculated results are listed in Table S3. (c) Log−log plot of water oxidation rate vs surface hole density at fixed [H$_2$O]s of 0.4 and 4 M measured at a fixed applied potential of 0.6 V$_{Ag/Ag^+}$. In both cases, a 470 nm LED irradiation was used from 50 to 300 mW cm^{-2} in 0.1 M TBAPF$_6$ solutions. The fitted EIS parameters and calculated results are listed in Tables S11 and S12.

TOF was also calculated from reaction activities and surface hole densities (Figures S13 and S14). The TOF results showed two regions around TWC, corresponding to the quasizero-order and half-order kinetics of H$_2$O, respectively (Figure S14). It has been reported that the incident light intensity influenced the surface hole density on α-Fe$_2$O$_3$ and caused a mechanistic transition from first to third order of surface holes for water oxidation on α-Fe$_2$O$_3$.[30,31] The first-order mechanism showed an activation energy (E_a) of 0.30 eV, while the third-order reaction mechanism had a very low E_a of 0.06 eV. Therefore, the enhanced surface hole densities under a high light intensity significantly reduced the activation energy barriers of RDS for water oxidation. The sequence between PT and ET is determined by the relative driving forces between the two steps.[8] The increased light intensity caused a higher driving force for ET and thus induced a transition from SPET to CPET (Figure 1a).

To further confirm that OH$^-$ ions are the real direct reactant for water oxidation, we purposely introduced OH$^-$ ions into the electrolyte, where TBAOH was used as the source of OH$^-$ ions. At low [OH$^-$] (0.1−2 mM), a quasi-zero-order was observed for OH$^-$ (Figure 2a), which was similar to that of H$_2$O at low [H$_2$O] as shown in Figure 1b. At high [OH$^-$] (2−16 mM), however, first-order kinetics appeared (Figure 2a), which could be assigned to the direct OH$^-$ oxidation involved in water oxidation. We further investigated the reaction order of H$_2$O in the presence of additional H$^+$ or OH$^-$. As shown in Figure 2b, the addition of 0.1 mM HClO$_4$ and 0.1 mM

TBAOH did not change the reaction order of H$_2$O when compared to the pristine condition. When the concentration of TBAOH was further increased to 2 mM, the reaction order of H$_2$O changed significantly. At low [H$_2$O] (0.1 to 0.8 M), the reaction rates were also independent of [H$_2$O] (slope = 0), but the rates were more prominent than that of the pristine condition (Figure 2b), indicating that the added OH$^-$ ions were the dominant reactants involved in the oxidation reaction. Above 0.8 M, the reaction rates increased slowly with the increase of [H$_2$O] with slope = 0.2 (Figure 2b), which was significantly lower than slope of 0.5 in 0.1 mM TBAOH. It can be roughly estimated that the concentration of OH$^-$ ions (dissociated from H$_2$O) that dominated in the SPET pathway was in the range from 0.1 to 2 mM.

In the mixed CH$_3$CN/H$_2$O electrolyte, [H$_2$O] influences the water oxidation rate by three effects. First, H$_2$O is the prereactant that generates OH$^-$ (Figure 3a) to take part in water oxidation as demonstrated above; second, H$_2$O/OH$^-$ themselves act as the proton acceptor in the PCET reaction; third, [H$_2$O] controls the surface hole density as the generation of surface high-valent Fe−O species (e.g., Fe^{IV}=O) must be assisted by H$_2$O (Figure 3a). We investigated the surface hole density by EIS under various [H$_2$O]s. At low [H$_2$O], the surface hole density gradually increased with [H$_2$O] (slope = 0.45) (Figure 3b). After [H$_2$O] reached 0.8 M, the surface hole density remained constant with [H$_2$O], and this TWC point was the same as that of water oxidation rate versus [H$_2$O] (Figure 3b). This constant surface hole density
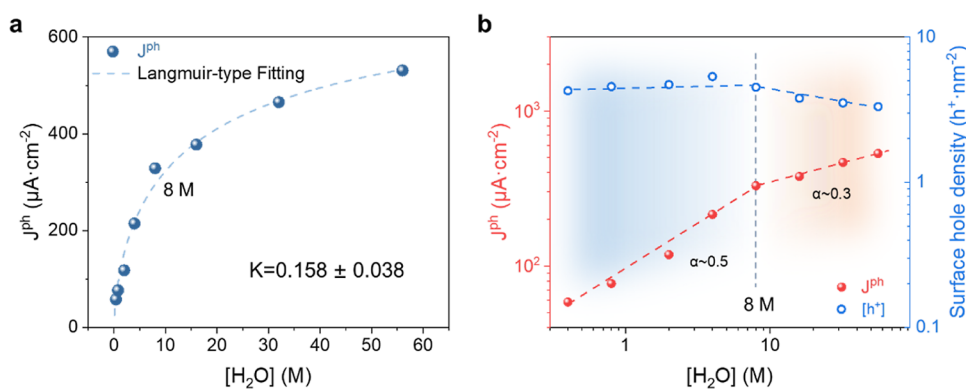
Figure 4. Comparison of the water oxidation mechanism in a nonaqueous solvent and in an aqueous solvent. (a) Plot of water oxidation rate as a function of $[H_2O]$ in 0.1 M $LiClO_4$ solutions at the applied potential of 0.9 V_{SCE} under the 470 nm LED illumination of 300 mW cm^{-2}. The dashed lines correspond to the fitting of the Langmuir isotherm curve. (b) Log–log plots of the water oxidation rate and surface hole density vs $[H_2O]$ in 0.1 M $LiClO_4$ solutions at the applied potential of 0.9 V_{SCE} under the 470 nm LED illumination of 300 mW cm^{-2}. In both cases, $[H_2O]$ of 56 M presented the aqueous solvent. The fitted EIS parameters and calculated results are listed in Table S13.
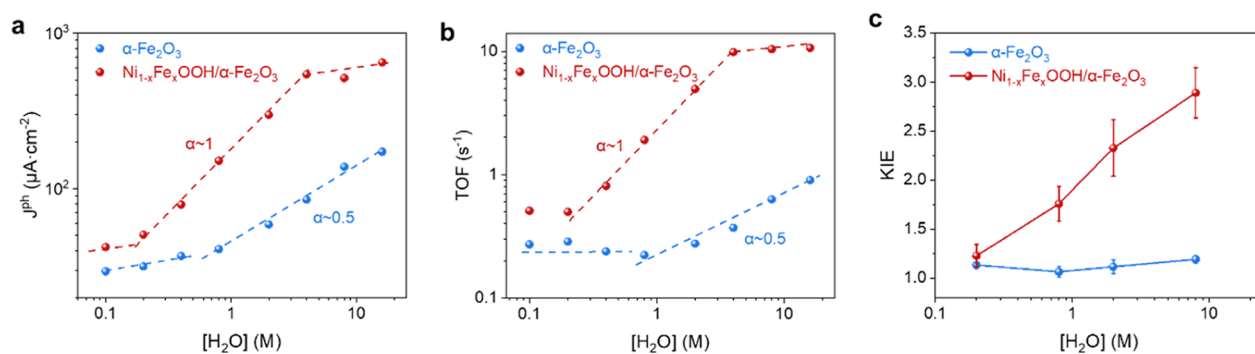

Figure 5. Surface modification of $Ni_{1-x}Fe_xOOH$ on α-Fe_2O_3 photoanodes. (a) Log–log plots of the water oxidation reaction rate vs $[H_2O]$ at the applied potential of 0.6 V_{Ag/Ag^+} under the 470 nm LED illumination of 100 mW cm^{-2}. (b) Log–log plots of the TOFs as a function of $[H_2O]$ in 0.1 M $TBAPF_6$ solutions under the 470 nm LED illumination of 100 mW cm^{-2}. (c) Comparison of the KIE results between pristine α-Fe_2O_3 and $Ni_{1-x}Fe_xOOH/\alpha$-Fe_2O_3 at different $[H_2O]$s and $[D_2O]$s.

with $[H_2O]$ above 0.8 M enabled us to perform a rational rate law analysis for H_2O molecules based on eq 1.

We further estimated the reaction order of surface holes at the two regions that was separated by TWC. At the low $[H_2O]$ of 0.4 M, a first-order kinetics of surface holes was observed for water oxidation, while a second-order kinetics of surface holes appeared at the high $[H_2O]$ of 4 M (Figures 3c, S15, and S16). This result confirmed that increasing $[H_2O]$ facilitated the surface hole-trapping process, which caused a transition from isolated to adjacent surface-trapped holes on α-Fe_2O_3. Based on the above results, eq 1 at the high $[H_2O]$ can be rewritten as

$$J^{ph} = k'[H_2O]^{0.5} \tag{2}$$

$$k' = k_{wo}[h^+]^2 \tag{3}$$

where k' is the apparent rate constant and is independent of $[H_2O]$. The calculated k_{wo} was 0.125 $holes^{-1}$ nm^2 $M^{-0.5}$ s^{-1}.

2.2. Comparison between the Nonaqueous Solvent and the Aqueous Solvent. In the discussion presented above, a SPET pathway for water oxidation on α-Fe_2O_3 was established in the mixed CH_3CN/H_2O electrolytes (Figure 3a). It is pivotal to correlate the reaction pathways of water oxidation in the nonaqueous solvent with that in the aqueous solvent. We further expanded $[H_2O]$ from 0.4 M (TWC) to 56 M (aqueous solvent) and explored its influence on the water

oxidation rate. As shown in Figure 4a, the distribution of water oxidation rates was divided into a rapidly increasing region and a slowly increasing region by the $[H_2O]$ of 8 M, which was consistent with the two distinct regions of H_2O reaction orders (Figure 4b). In the entire $[H_2O]$ region, the overall J^{ph}–$[H_2O]$ can be well fitted by a single Langmuir isotherm curve (for details, see Supporting Information Note 4), indicating that the reaction rate is determined by the surface coverage of H_2O. The slow increasing region at high $[H_2O]$ is because the adsorption of H_2O reached saturation under this condition. On the other hand, above $[H_2O]$ of 8 M, the surface hole density slightly decreased with $[H_2O]$, indicating that further increasing $[H_2O]$ facilitated the consumption of surface holes and thus contributed to the further slow increase of water oxidation. From these results, we can infer that below $[H_2O]$ of 8 M, OH^- is the dominate reactant involved in water oxidation, while the contribution of H_2O as a direct reactant becomes more and more significant with increasing $[H_2O]$ above 8 M. In the aqueous solvent ($[H_2O]$ of 56 M), the oxidation of both OH^- and H_2O contributes to the water oxidation activity, in which the amount of H_2O is much higher than that of OH^-, but the reaction kinetics of OH^- is substantially faster. The reaction kinetics of H_2O oxidation and OH^- oxidation were calculated to be 5.56×10^{-16} and 8.73×10^{-1} s^{-1}, respectively, according to the theoretical results by Piccinin et al.[32] Therefore, H_2O dissociation and oxidation of
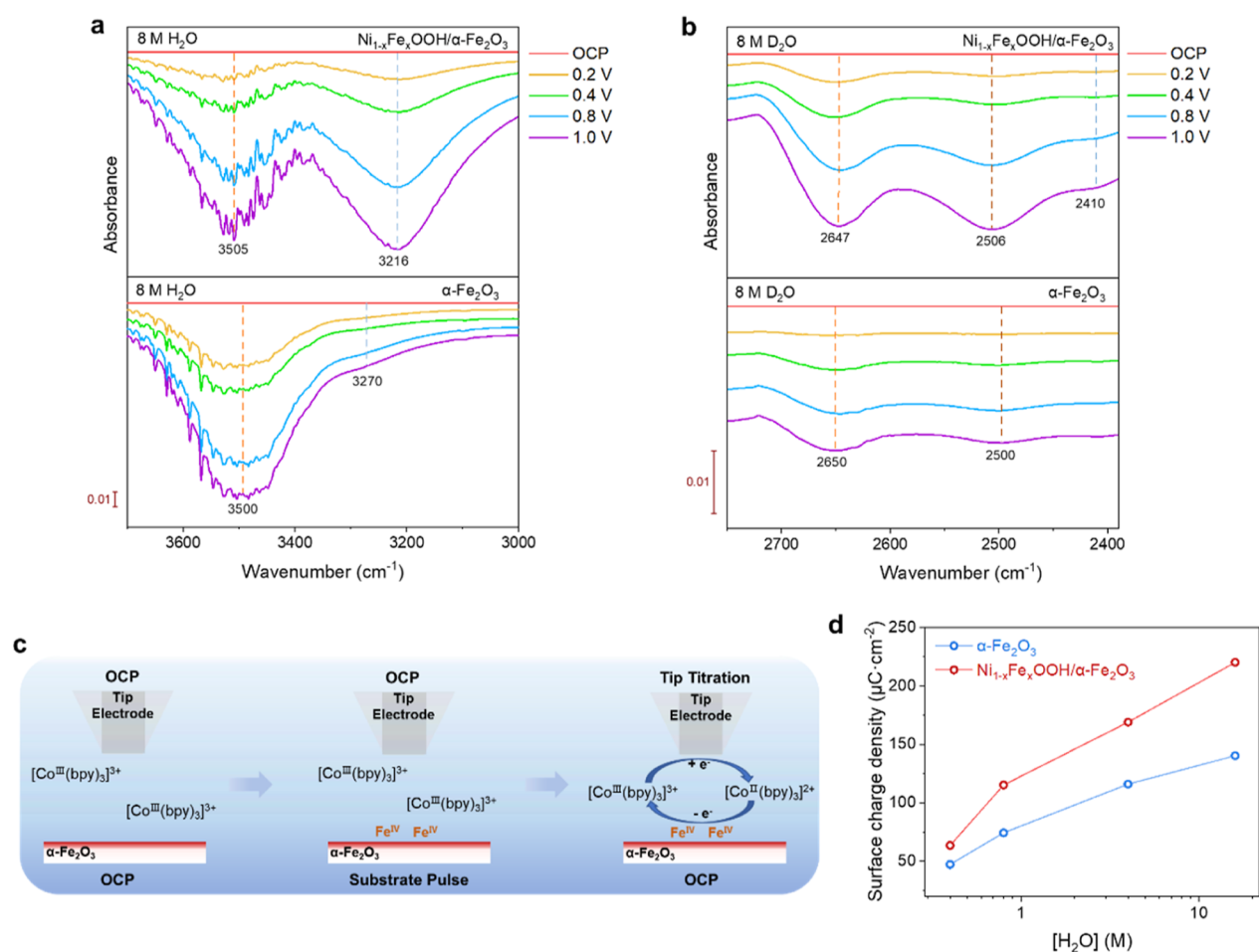
Figure 6. Operando spectroscopic studies. ATR−FTIR spectra recorded in the potential range from the OCP to 1.0 V vs Ag/Ag$^+$ on α-Fe$_2$O$_3$ and Ni$_{1−x}$Fe$_x$OOH/α-Fe$_2$O$_3$ at (a) [H$_2$O] of 8 M and (b) [D$_2$O] of 8 M. The reference spectra were taken under the OCP condition. (c) Redox titration sequence for the SI-SECM experiment to quantitatively analyze the surface hole density on the substrate. (d) Surface charge density calculated by the titration curves at various [H$_2$O]s.

the resulted OH$^−$ play an essential role in both nonaqueous and aqueous solvents, and this work provides an effective method to study this.

2.3. Surface Modification of Ni$_{1−x}$Fe$_x$OOH. Under low to moderate light intensity illumination, the SPET pathway dominates the water oxidation on α-Fe$_2$O$_3$ in the mixed CH$_3$CN/H$_2$O electrolytes. However, the maximum concentration of OH$^−$ ions dissociated by H$_2$O is only about 0.1 mM in the mixed electrolyte, which greatly limits the rate of reaction of water oxidation. Therefore, it is urgently needed to involve H$_2$O as the direct water-oxidation reactant for further improving water oxidation performance of semiconductor photoanodes. Under this circumstance, further optimizations on the material PEC properties (e.g., light absorption, charge separation) will be less important. Seeking a surface modification layer that possesses the CPET pathway of H$_2$O is more promising, but very few previously reported modification methods (e.g., doping or heterojunctions) have shown the ability to alter the PCET pathway of water oxidation on semiconductor photoanodes. Figures 1b and S9 show that both Ni$_{1−x}$Fe$_x$OOH modification and the Ni$_{1−x}$Fe$_x$OOH electrocatalyst itself caused a first-order kinetics of H$_2$O, suggesting that the Ni$_{1−x}$Fe$_x$OOH electrocatalyst might be the key to involving H$_2$O as the direct water-oxidation reactant. Ni$_{1−x}$Fe$_x$OOH-modified α-Fe$_2$O$_3$ (labeled as Ni$_{1−x}$Fe$_x$OOH/

α-Fe$_2$O$_3$) was thus fabricated, and the structural characterizations are shown in Figure S17. LSV curves of Ni$_{1−x}$Fe$_x$OOH/α-Fe$_2$O$_3$ under various [H$_2$O]s are shown in Figure S18. Ni$_{1−x}$Fe$_x$OOH/α-Fe$_2$O$_3$ showed a first-order kinetics of H$_2$O at moderate [H$_2$O] (0.2−4 M) and reached saturation above [H$_2$O] of 4 M (Figure 5a and S19). Meanwhile, the water oxidation rate and TOF were accelerated by 1 order of magnitude after Ni$_{1−x}$Fe$_x$OOH modification (Figures 5b and S20). On the other hand, H/D KIE experiments were conducted to probe PT in the RDS of water oxidation. On the pristine α-Fe$_2$O$_3$, a low KIE value of 1.1−1.2 was observed (Figure 5c), which is consistent with the SPET pathway that PT is not involved in the RDS. In contrast, the Ni$_{1−x}$Fe$_x$OOH modification greatly improved the KIE value to 2−2.5 (Figure 5c), which is the direct evidence that PT is indeed involved in the RDS of water oxidation. It confirms the mechanistic transition from SPET to CPET upon Ni$_{1−x}$Fe$_x$OOH modification. It is the first time that a Ni$_{1−x}$Fe$_x$OOH electrocatalyst is found to be a PCET modulator.

To further identify the PCET pathway for water oxidation, the surface species during PEC water oxidation were probed by operando ATR−FTIR measurements on α-Fe$_2$O$_3$ and Ni$_{1−x}$Fe$_x$OOH/α-Fe$_2$O$_3$ photoanodes. Figures S21 and S22 show the IR spectra of pure H$_2$O and mixed CH$_3$CN/H$_2$O
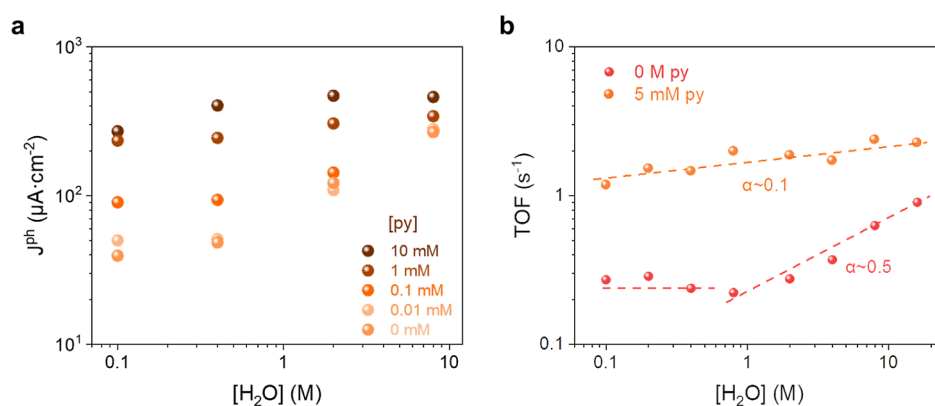
Figure 7. Influence of a proton acceptor (pyridine) on the rate law of H_2O. (a) Log−log plot of the water oxidation reaction rate vs $[H_2O]$ in 0.1 M $TBAPF_6$ solutions with different concentrations of pyridine at the applied potential of 0.6 V_{Ag/Ag^+} measured under the 470 nm LED illumination of 100 mW cm^{-2}. (b) Comparison of the TOFs in 0.1 M $TBAPF_6$ solutions with and without pyridine.

solutions on α-Fe_2O_3 and $Ni_{1-x}Fe_xOOH/\alpha$-Fe_2O_3 photoanodes. Figure 6a shows the IR spectra acquired from the open-circuit potential (OCP) to 1.0 V_{Ag/Ag^+} on α-Fe_2O_3 and $Ni_{1-x}Fe_xOOH/\alpha$-Fe_2O_3 photoanodes at $[H_2O]$ of 8 M under 470 nm LED illumination. For the α-Fe_2O_3 photoanode, the broad negative band at ~3500 cm^{-1} consisted of the symmetric and asymmetric stretching vibrations of surface-adsorbed OH (Figure S23),[42,43] showing the consumption of surface-adsorbed OH on α-Fe_2O_3 during water oxidation. This was consistent with the KIE results that show that water oxidation on α-Fe_2O_3 occurred via the SPET pathway in the mixed CH_3CN/H_2O electrolytes. The negative bands at ~3270 cm^{-1} on the α-Fe_2O_3 photoanode and at ~3216 cm^{-1} on the $Ni_{1-x}Fe_xOOH/\alpha$-Fe_2O_3 photoanode were assigned to the O−H stretching vibration of hydrogen-bonded H_2O molecules.[43,44] It can be seen that the consumption of hydrogen-bonded H_2O molecules on the $Ni_{1-x}Fe_xOOH/\alpha$-Fe_2O_3 surface was much more predominant than that on the α-Fe_2O_3 surface. This result confirms that the H_2O molecules as the direct reactant are involved in water oxidation on $Ni_{1-x}Fe_xOOH/\alpha$-Fe_2O_3 photoanodes, validating the mechanistic transition from SPET to CPET upon $Ni_{1-x}Fe_xOOH$ modification. The same ATR−FTIR measurements were conducted in the mixed CH_3CN/D_2O electrolyte to confirm the above assignments. The negative-going bands at around ~2650 and ~2500 cm^{-1} were associated with asymmetric and symmetric stretching vibrations of surface-adsorbed OD on α-Fe_2O_3 and $Ni_{1-x}Fe_xOOH/\alpha$-Fe_2O_3 surfaces (Figure 6b and S22d). The $Ni_{1-x}Fe_xOOH/\alpha$-Fe_2O_3 photoanode showed an additional band at ~2400 cm^{-1}, which was assigned to the O−D stretching vibration of deuterium-bonded D_2O molecules on surfaces, confirming the consumption of hydrogen-bonded H_2O molecules on $Ni_{1-x}Fe_xOOH/\alpha$-Fe_2O_3 surfaces. The IR results demonstrate that pristine α-Fe_2O_3 can oxidize adsorbed OH from dissociative adsorption of H_2O, while both hydrogen-bonded H_2O molecules and adsorbed OH can be oxidized by $Ni_{1-x}Fe_xOOH/\alpha$-Fe_2O_3.

The previous study on the $Ni_{1-x}Fe_xOOH$ electrocatalyst proposed the presence of high-valent Fe(VI) species on surfaces.[45,46] Therefore, it can be concluded that $Ni_{1-x}Fe_xOOH$ surfaces possess stronger oxidation ability than α-Fe_2O_3 surfaces, which facilitates the CPET pathway. Herein, we used SI-SECM measurements to titrate and compare the surface hole densities of the pristine and $Ni_{1-x}Fe_xOOH$-modifed α-Fe_2O_3 photoanodes. To exclude

the effect of enhanced oxygen evolution kinetics by $Ni_{1-x}Fe_xOOH$, the titration was performed under OCP conditions following the surface hole-trapping process under PEC conditions (Figure 6c). ($[Co^{II}(bpy)_3]^{2+}$) was used as the titration to quantify the surface holes' density on the photoanodes, which can compete with the water oxidation reaction for consuming the surface holes.[47] More details are shown in Figures S24 and S25. The titration curves are shown in Figure S26. The calculated surface charge density of $Ni_{1-x}Fe_xOOH/\alpha$-Fe_2O_3 was much higher than that of pristine α-Fe_2O_3 (Figure 6d). For example, the surface charge density reached 115.3 μC cm^{-2} for $Ni_{1-x}Fe_xOOH/\alpha$-Fe_2O_3, while pristine α-Fe_2O_3 only showed 74.4 μC cm^{-2} at a $[H_2O]$ of 0.8 M (Figure 6d). The greatly increased surface hole density caused a stronger oxidation ability.

2.4. Role of Proton Acceptors. In the mixed electrolyte, H_2O plays the role of a proton acceptor as the dissociated $[OH^-]$ is low, but H_2O is a poor proton acceptor.[22] Therefore, introducing stronger proton acceptors to the electrolyte for facilitating PT is considered an effective way to enhance the water oxidation performance. Herein, pyridine was selected as an effective proton acceptor with Faraday efficiencies of O_2 > 90% (Figure S27). As shown in Figure 7a, the presence of pyridine greatly enhanced the water oxidation rate at low $[H_2O]$. For example, the water oxidation rate at $[H_2O]$ of 0.1 M with only 1 mM of pyridine reached a high level at $[H_2O]$ of 16 M without pyridine. As a result, the reaction order of H_2O exhibited a quasi-zero-order kinetics in the presence of 1 and 10 mM of pyridine (Figure 7a).

The role of pyridine in improving the water oxidation performance is further investigated by the rate law analysis of surface holes. A second-order kinetics of surface holes was observed at low $[H_2O]$ of 0.4 M (Figure S28), indicating that the addition of pyridine promoted the generation of adjacent surface-trapped holes by accelerating the PT during the oxidation of Fe−OH. The presence of adjacent surface-trapped holes in turn provides a stronger driving force for ET during the subsequent H_2O oxidation by surface holes and thus causes the almost 1 order of magnitude enhancement in TOFs at low $[H_2O]$ (Figures 7b and S29).

3. CONCLUSIONS

By conducting rate law analysis of H_2O molecules, we reveal a universal SPET pathway for water oxidation on five typical photoanodes, which is the rate-limiting factor that causes the

sluggish water oxidation performance. This SPET pathway indicates that H$_2$O molecules do not directly participate in the water oxidation process. But the OH$^-$ dissociated from H$_2$O is indeed the direct reactant. Besides, this reaction mechanism of water oxidation in a nonaqueous solvent can be extended to the aqueous solvent by fitting of the single Langmuir isotherm curve. Further surface modification of a well-known electrocatalyst, Ni$_{1-x}$Fe$_x$OOH, was found to induce a mechanistic transition from the SPET to the CPET pathway, as evidenced by H/D KIE, operando ATR−FTIR, and SI-SECM studies, and the TOF of water oxidation was enhanced by 1 order of magnitude. It is the first time that the Ni$_{1-x}$Fe$_x$OOH electrocatalyst is found to be a PCET modulator. Besides, the PT process can be regulated by using the proton acceptor (pyridine), which significantly improved the TOF at low [H$_2$O] to that in the aqueous solvent. This work illustrates an effective strategy for modulating PCET kinetics of water oxidation on semiconductor surfaces.

ASSOCIATED CONTENT

Supporting Information

The Supporting Information is available free of charge at https://pubs.acs.org/doi/10.1021/jacs.3c09410.

Experimental details of samples' fabrication and characterization; calibration of the potentials (vs Ag/Ag$^+$ and SCE) with the ferrocene/ferrocenium (Fc/Fc$^+$) redox couple in a nonaqueous solvent; calculation of the surface-trapped hole density and the reaction order of surface hole density; current−voltage curves of samples; analysis of the diffusion step for the water oxidation reaction; Faradaic efficiency measurements; characterization data of Ni$_{1-x}$Fe$_x$OOH/α-Fe$_2$O$_3$; operando ATR−FTIR and SI-SECM measurements; fitted EIS data; and discussions on the surface hole density with [H$_2$O] and on values of the reaction order of H$_2$O (PDF)

AUTHOR INFORMATION

Corresponding Author
Yuchao Zhang − Key Laboratory of Photochemistry, CAS Research/Education Center for Excellence in Molecular Sciences, Institute of Chemistry, Chinese Academy of Sciences, Beijing 100190, P. R. China; University of Chinese Academy of Sciences, Beijing 100049, P. R. China; orcid.org/0000-0003-3215-1033; Email: yczhang@iccas.ac.cn

Authors
Siqin Liu − Key Laboratory of Photochemistry, CAS Research/Education Center for Excellence in Molecular Sciences, Institute of Chemistry, Chinese Academy of Sciences, Beijing 100190, P. R. China; University of Chinese Academy of Sciences, Beijing 100049, P. R. China

Lei Wu − Key Laboratory of Photochemistry, CAS Research/Education Center for Excellence in Molecular Sciences, Institute of Chemistry, Chinese Academy of Sciences, Beijing 100190, P. R. China; University of Chinese Academy of Sciences, Beijing 100049, P. R. China

Daojian Tang − Key Laboratory of Photochemistry, CAS Research/Education Center for Excellence in Molecular Sciences, Institute of Chemistry, Chinese Academy of Sciences, Beijing 100190, P. R. China; University of Chinese Academy of Sciences, Beijing 100049, P. R. China

Jing Xue − Key Laboratory of Photochemistry, CAS Research/Education Center for Excellence in Molecular Sciences, Institute of Chemistry, Chinese Academy of Sciences, Beijing 100190, P. R. China; University of Chinese Academy of Sciences, Beijing 100049, P. R. China

Kun Dang − Key Laboratory of Photochemistry, CAS Research/Education Center for Excellence in Molecular Sciences, Institute of Chemistry, Chinese Academy of Sciences, Beijing 100190, P. R. China; University of Chinese Academy of Sciences, Beijing 100049, P. R. China

Hanbin He − Key Laboratory of Photochemistry, CAS Research/Education Center for Excellence in Molecular Sciences, Institute of Chemistry, Chinese Academy of Sciences, Beijing 100190, P. R. China; University of Chinese Academy of Sciences, Beijing 100049, P. R. China

Shuming Bai − Key Laboratory of Photochemistry, CAS Research/Education Center for Excellence in Molecular Sciences, Institute of Chemistry, Chinese Academy of Sciences, Beijing 100190, P. R. China; University of Chinese Academy of Sciences, Beijing 100049, P. R. China; orcid.org/0000-0002-4993-8070

Hongwei Ji − Key Laboratory of Photochemistry, CAS Research/Education Center for Excellence in Molecular Sciences, Institute of Chemistry, Chinese Academy of Sciences, Beijing 100190, P. R. China; University of Chinese Academy of Sciences, Beijing 100049, P. R. China

Chuncheng Chen − Key Laboratory of Photochemistry, CAS Research/Education Center for Excellence in Molecular Sciences, Institute of Chemistry, Chinese Academy of Sciences, Beijing 100190, P. R. China; University of Chinese Academy of Sciences, Beijing 100049, P. R. China; orcid.org/0000-0003-4034-8063

Jincai Zhao − Key Laboratory of Photochemistry, CAS Research/Education Center for Excellence in Molecular Sciences, Institute of Chemistry, Chinese Academy of Sciences, Beijing 100190, P. R. China; University of Chinese Academy of Sciences, Beijing 100049, P. R. China; orcid.org/0000-0003-1449-4235

Complete contact information is available at:
https://pubs.acs.org/10.1021/jacs.3c09410

Author Contributions
§S.L. and L.W. contributed equally.

Notes
The authors declare no competing financial interest.

REFERENCES
(1) Wang, Q.; Domen, K. Particulate Photocatalysts for Light-Driven Water Splitting: Mechanisms, Challenges, and Design Strategies. *Chem. Rev.* **2020**, *120* (2), 919−985.
(2) Huynh, M. H. V.; Meyer, T. J. Proton-Coupled Electron Transfer. *Chem. Rev.* **2007**, *107* (11), 5004−5064.
(3) Chen, J.; Li, Y. F.; Sit, P.; Selloni, A. Chemical dynamics of the first proton-coupled electron transfer of water oxidation on TiO$_2$ anatase. *J. Am. Chem. Soc.* **2013**, *135* (50), 18774−18777.

(4) Corby, S.; Rao, R. R.; Steier, L.; Durrant, J. R. The kinetics of metal oxide photoanodes from charge generation to catalysis. *Nat. Rev. Mater.* **2021**, *6* (12), 1136−1155.

(5) Costentin, C. Electrochemical approach to the mechanistic study of proton-coupled electron transfer. *Chem. Rev.* **2008**, *108* (7), 2145−2179.

(6) Hammes-Schiffer, S.; Stuchebrukhov, A. A. Theory of Coupled Electron and Proton Transfer Reactions. *Chem. Rev.* **2010**, *110* (12), 6939−6960.

(7) Weinberg, D. R.; Gagliardi, C. J.; Hull, J. F.; Murphy, C. F.; Kent, C. A.; Westlake, B. C.; Paul, A.; Ess, D. H.; McCafferty, D. G.; Meyer, T. J. Proton-coupled electron transfer. *Chem. Rev.* **2012**, *112* (7), 4016−4093.

(8) Tyburski, R.; Liu, T.; Glover, S. D.; Hammarstrom, L. Proton-Coupled Electron Transfer Guidelines, Fair and Square. *J. Am. Chem. Soc.* **2021**, *143* (2), 560−576.

(9) Umena, Y.; Kawakami, K.; Shen, J. R.; Kamiya, N. Crystal structure of oxygen-evolving photosystem II at a resolution of 1.9 A. *Nature* **2011**, *473* (7345), 55−60.

(10) Tachibana, Y.; Vayssieres, L.; Durrant, J. R. Artificial photosynthesis for solar water-splitting. *Nat. Photonics* **2012**, *6* (8), 511−518.

(11) Lin, F.; Boettcher, S. W. Adaptive semiconductor/electrocatalyst junctions in water-splitting photoanodes. *Nat. Mater.* **2014**, *13* (1), 81−86.

(12) Ye, S.; Ding, C.; Liu, M.; Wang, A.; Huang, Q.; Li, C. Water Oxidation Catalysts for Artificial Photosynthesis. *Adv. Mater.* **2019**, *31* (50), 1902069.

(13) Guan, J.; Duan, Z.; Zhang, F.; Kelly, S. D.; Si, R.; Dupuis, M.; Huang, Q.; Chen, J. Q.; Tang, C.; Li, C. Water oxidation on a mononuclear manganese heterogeneous catalyst. *Nat. Catal.* **2018**, *1* (11), 870−877.

(14) Barber, J. Photosynthetic energy conversion: natural and artificial. *Chem. Soc. Rev.* **2009**, *38* (1), 185−196.

(15) Schulze, M.; Kunz, V.; Frischmann, P. D.; Wurthner, F. A supramolecular ruthenium macrocycle with high catalytic activity for water oxidation that mechanistically mimics photosystem II. *Nat. Chem.* **2016**, *8* (6), 576−583.

(16) Okamura, M.; Kondo, M.; Kuga, R.; Kurashige, Y.; Yanai, T.; Hayami, S.; Praneeth, V. K.; Yoshida, M.; Yoneda, K.; Kawata, S.; Masaoka, S. A pentanuclear iron catalyst designed for water oxidation. *Nature* **2016**, *530* (7591), 465−468.

(17) Allgower, F.; Gamiz-Hernandez, A. P.; Rutherford, A. W.; Kaila, V. R. I. Molecular Principles of Redox-Coupled Protonation Dynamics in Photosystem II. *J. Am. Chem. Soc.* **2022**, *144* (16), 7171−7180.

(18) Guo, Y.; Messinger, J.; Kloo, L.; Sun, L. Reversible Structural Isomerization of Nature's Water Oxidation Catalyst Prior to O-O Bond Formation. *J. Am. Chem. Soc.* **2022**, *144* (26), 11736−11747.

(19) Hussein, R.; Ibrahim, M.; Bhowmick, A.; Simon, P. S.; Chatterjee, R.; Lassalle, L.; Doyle, M.; Bogacz, I.; Kim, I. S.; Cheah, M. H.; Gul, S.; de Lichtenberg, C.; Chernev, P.; Pham, C. C.; Young, I. D.; Carbajo, S.; Fuller, F. D.; Alonso-Mori, R.; Batyuk, A.; Sutherlin, K. D.; Brewster, A. S.; Bolotovsky, R.; Mendez, D.; Holton, J. M.; Moriarty, N. W.; Adams, P. D.; Bergmann, U.; Sauter, N. K.; Dobbek, H.; Messinger, J.; Zouni, A.; Kern, J.; Yachandra, V. K.; Yano, J. Structural dynamics in the water and proton channels of photosystem II during the S_2 to S_3 transition. *Nat. Commun.* **2021**, *12* (1), 6531−6547.

(20) Barber, J. A mechanism for water splitting and oxygen production in photosynthesis. *Nat. Plants* **2017**, *3*, 17041−17045.

(21) Cheng, J.; Liu, X.; Kattirtzi, J. A.; VandeVondele, J.; Sprik, M. Aligning electronic and protonic energy levels of proton-coupled electron transfer in water oxidation on aqueous TiO_2. *Angew. Chem., Int. Ed. Engl.* **2014**, *53* (45), 12046−12050.

(22) Zhang, Y.; Zhang, H.; Ji, H.; Ma, W.; Chen, C.; Zhao, J. Pivotal Role and Regulation of Proton Transfer in Water Oxidation on Hematite Photoanodes. *J. Am. Chem. Soc.* **2016**, *138* (8), 2705−2711.

(23) Grimaud, A.; Diaz-Morales, O.; Han, B.; Hong, W. T.; Lee, Y. L.; Giordano, L.; Stoerzinger, K. A.; Koper, M. T. M.; Shao-Horn, Y. Activating lattice oxygen redox reactions in metal oxides to catalyse oxygen evolution. *Nat. Chem.* **2017**, *9* (5), 457−465.

(24) Zhang, Y.; Zhang, H.; Liu, A.; Chen, C.; Song, W.; Zhao, J. Rate-Limiting O-O Bond Formation Pathways for Water Oxidation on Hematite Photoanode. *J. Am. Chem. Soc.* **2018**, *140* (9), 3264−3269.

(25) Yang, S.; Li, X.; Li, Y.; Wang, Y.; Jin, X.; Qin, L.; Zhang, W.; Cao, R. Effect of Proton Transfer on Electrocatalytic Water Oxidation by Manganese Phosphates. *Angew. Chem., Int. Ed.* **2022**, *62* (1), No. e202215594.

(26) Mayer, J. M. Bonds over Electrons: Proton Coupled Electron Transfer at Solid-Solution Interfaces. *J. Am. Chem. Soc.* **2023**, *145* (13), 7050−7064.

(27) Chen, C.; Shi, T.; Chang, W.; Zhao, J. Essential Roles of Proton Transfer in Photocatalytic Redox Reactions. *ChemCatChem* **2015**, *7* (5), 724−731.

(28) Loget, G.; Fabre, B.; Fryars, S.; Mériadec, C.; Ababou-Girard, S. Dispersed Ni Nanoparticles Stabilize Silicon Photoanodes for Efficient and Inexpensive Sunlight-Assisted Water Oxidation. *ACS Energy Lett.* **2017**, *2* (3), 569−573.

(29) Ma, Y.; Mesa, C. A.; Pastor, E.; Kafizas, A.; Francàs, L.; Le Formal, F.; Pendlebury, S. R.; Durrant, J. R. Rate Law Analysis of Water Oxidation and Hole Scavenging on a $BiVO_4$ Photoanode. *ACS Energy Lett.* **2016**, *1* (3), 618−623.

(30) Le Formal, F.; Pastor, E.; Tilley, S. D.; Mesa, C. A.; Pendlebury, S. R.; Gratzel, M.; Durrant, J. R. Rate law analysis of water oxidation on a hematite surface. *J. Am. Chem. Soc.* **2015**, *137* (20), 6629−6637.

(31) Mesa, C. A.; Francas, L.; Yang, K. R.; Garrido-Barros, P.; Pastor, E.; Ma, Y.; Kafizas, A.; Rosser, T. E.; Mayer, M. T.; Reisner, E.; Gratzel, M.; Batista, V. S.; Durrant, J. R. Multihole water oxidation catalysis on haematite photoanodes revealed by operando spectroelectrochemistry and DFT. *Nat. Chem.* **2020**, *12* (1), 82−89.

(32) Righi, G.; Plescher, J.; Schmidt, F.-P.; Campen, R. K.; Fabris, S.; Knop-Gericke, A.; Schlögl, R.; Jones, T. E.; Teschner, D.; Piccinin, S. On the origin of multihole oxygen evolution in haematite photoanodes. *Nat. Catal.* **2022**, *5* (10), 888−899.

(33) Zandi, O.; Hamann, T. W. Determination of photoelectrochemical water oxidation intermediates on haematite electrode surfaces using operando infrared spectroscopy. *Nat. Chem.* **2016**, *8* (8), 778−783.

(34) Lewis, N. S. Progress in Understanding Electron-Transfer Reactions at Semiconductor/Liquid Interfaces. *J. Phys. Chem. B* **1998**, *102* (25), 4843−4855.

(35) Yang, X.; Wang, Y.; Li, C. M.; Wang, D. Mechanisms of water oxidation on heterogeneous catalyst surfaces. *Nano Res.* **2021**, *14* (10), 3446−3457.

(36) Blakemore, J. D.; Crabtree, R. H.; Brudvig, G. W. Molecular Catalysts for Water Oxidation. *Chem. Rev.* **2015**, *115* (23), 12974−13005.

(37) Li, X.; Zhang, X. P.; Guo, M.; Lv, B.; Guo, K.; Jin, X.; Zhang, W.; Lee, Y. M.; Fukuzumi, S.; Nam, W.; Cao, R. Identifying Intermediates in Electrocatalytic Water Oxidation with a Manganese Corrole Complex. *J. Am. Chem. Soc.* **2021**, *143* (36), 14613−14621.

(38) Zhang, C.; Chen, C.; Dong, H.; Shen, J.-R.; Dau, H.; Zhao, J. A synthetic Mn_4Ca-cluster mimicking the oxygen-evolving center of photosynthesis. *Science* **2015**, *348* (6235), 690−693.

(39) Hemmerling, J. R.; Mathur, A.; Linic, S. Design Principles for Efficient and Stable Water Splitting Photoelectrocatalysts. *Acc. Chem. Res.* **2021**, *54* (8), 1992−2002.

(40) Luo, Z.; Wang, T.; Gong, J. Single-crystal silicon-based electrodes for unbiased solar water splitting: current status and prospects. *Chem. Soc. Rev.* **2019**, *48* (7), 2158−2181.

(41) Hunter, B. M.; Gray, H. B.; Muller, A. M. Earth-Abundant Heterogeneous Water Oxidation Catalysts. *Chem. Rev.* **2016**, *116* (22), 14120−14136.

(42) Lange, K. M.; Hodeck, K. F.; Schade, U.; Aziz, E. F. Nature of the Hydrogen Bond of Water in Solvents of Different Polarities. *J. Phys. Chem. B* **2010**, *114* (50), 16997−17001.

(43) Al-Abadleh, H. A.; Grassian, V. H. FT-IR Study of Water Adsorption on Aluminum Oxide Surfaces. *Langmuir* **2003**, *19* (2), 341−347.

(44) Sheng, H.; Zhang, H.; Song, W.; Ji, H.; Ma, W.; Chen, C.; Zhao, J. Activation of Water in Titanium Dioxide Photocatalysis by Formation of Surface Hydrogen Bonds: An In Situ IR Spectroscopy Study. *Angew. Chem., Int. Ed. Engl.* **2015**, *54* (20), 5905−5909.

(45) Hunter, B. M.; Thompson, N. B.; Müller, A. M.; Rossman, G. R.; Hill, M. G.; Winkler, J. R.; Gray, H. B. Trapping an Iron(VI) Water-Splitting Intermediate in Nonaqueous Media. *Joule* **2018**, *2* (4), 747−763.

(46) Feng, C.; She, X.; Xiao, Y.; Li, Y. Direct Detection of Fe(VI) Water Oxidation Intermediates in an Aqueous Solution. *Angew. Chem., Int. Ed.* **2023**, *62*, No. e202218738.

(47) Kim, J. Y.; Ahn, H. S.; Bard, A. J. Surface Interrogation Scanning Electrochemical Microscopy for a Photoelectrochemical Reaction: Water Oxidation on a Hematite Surface. *Anal. Chem.* **2018**, *90* (5), 3045−3049.